



Cite this: *Energy Adv.*, 2024, 3, 1073

## Ag/Pd bimetallic nanoparticle-loaded Zr-MOF: an efficacious visible-light-responsive photocatalyst for H<sub>2</sub>O<sub>2</sub> and H<sub>2</sub> production†

Srabani Dash, Suraj Prakash Tripathy, Satyabrata Subudhi, Lopamudra Acharya, Asheli Ray, Pragyandeepi Behera and Kulamani Parida \*

Photocatalytic production of H<sub>2</sub>O<sub>2</sub> and H<sub>2</sub> holds promise for conquering the impending energy crisis. In order to accomplish this goal, the photocatalysts must be robust and effective enough to harvest photons from a wide solar spectrum as well as having a high rate of exciton antirecombination. Low visible light absorption and fast recombination of exciton pairs are two major setbacks encountered in pristine MOF-based photocatalysts. Herein, the MOF UiO-66-NH<sub>2</sub> modified with noble bimetallic nanoparticles (Ag/Pd) was synthesized via a facile adsorption–reduction technique and utilized for effective photocatalytic H<sub>2</sub>O<sub>2</sub> and H<sub>2</sub> production. The composite (1:2) Ag/Pd@UiO-66-NH<sub>2</sub> displayed a H<sub>2</sub>O<sub>2</sub> production rate of 39.4 μmol h<sup>-1</sup> in an O<sub>2</sub>-saturated environment in the presence of IPA and water under visible light illumination, which is almost four-fold more than that of the pristine UiO-66-NH<sub>2</sub> MOF and twofold greater than those of the monometallic counterparts (Ag@MOF or Pd@MOF). Moreover, the photocatalytic H<sub>2</sub> evolution of the prepared materials was studied and a similar trend was observed in which the composite (1:2) Ag/Pd@UiO-66-NH<sub>2</sub> showed the highest H<sub>2</sub> evolution capacity of 448.2 μmol h<sup>-1</sup>. The enhanced photocatalytic performance of the Ag/Pd@MOF composite can be attributed to its ability to suppress exciton recombination, superior photon reception, and fast charge transfer. Mechanistically the transfer of photogenerated electrons from the UiO-66-NH<sub>2</sub> surface to the bimetallic component was promoted through the LSPR effect of Ag and this is further enhanced by the Pd support. The electron-trapping capacity of the bimetallic nanoparticle (NP)-based co-catalyst enhances the overall reaction mechanism by giving highly surface active sites on the surface for the photocatalytic production of H<sub>2</sub>O<sub>2</sub> and H<sub>2</sub> as a sustainable means of green energy production.

Received 4th December 2023,  
Accepted 30th March 2024

DOI: 10.1039/d3ya00597f

rsc.li/energy-advances

Centre for Nano Science and Nanotechnology, Siksha 'O' Anusandhan (Deemed to be University), Bhubaneswar, Odisha, 751030, India.

E-mail: paridkulamani@yahoo.com, kulamaniparida@soa.ac.in;

Fax: +91-674-2350642; Tel: +91-674-2351777

† Electronic supplementary information (ESI) available: 1. Experimental techniques (1.1. Characterization techniques, 1.2. FTO preparation, and 1.3. Scavenger test procedure); Fig. S1: BET surface area and BJH pore size distribution of (1:2) Ag/Pd@UiO-66-NH<sub>2</sub>; Fig. S2: XPS survey spectra of UiO-66-NH<sub>2</sub> and (1:2) Ag/Pd@UiO-66-NH<sub>2</sub>; Fig. S3: PL plot for UiO-66-NH<sub>2</sub> and (1:1, 1:2, 2:1) Ag/Pd@UiO-66-NH<sub>2</sub>; Fig. S4: TRPL plot of (1:2) Ag/Pd@UiO-66-NH<sub>2</sub>; Fig. S5: LSV plot of the prepared photocatalysts; Fig. S6: Post photo-catalytic PXRD analysis; Table S1: TRPL data of UiO-66-NH<sub>2</sub> and (1:2) Ag/Pd@UiO-66-NH<sub>2</sub>; Table S2: apparent conversion efficiency (ACE) expression and calculation for photocatalytic hydrogen evolution by the prepared photocatalysts; Table S3: comparison of photocatalytic H<sub>2</sub>O<sub>2</sub> production by various photocatalysts; Table S4: comparison of photocatalytic H<sub>2</sub> evolution by various photocatalysts. See DOI: <https://doi.org/10.1039/d3ya00597f>

## 1. Introduction

Hydrogen peroxide (H<sub>2</sub>O<sub>2</sub>) is considered as a green and eco-friendly oxidant, which can be treated as an active oxidant, producing water as by-product, with potential for use in extensive applications, such as pollutant degradation, waste water treatment, chemical industry, sterilization, and other environmental applications. Recently, H<sub>2</sub>O<sub>2</sub> has also attracted a lot of attention as a promising energy carrier for fuel cells because it is water-soluble and can be used to generate electricity in a single-compartment cell.<sup>1,2</sup> Mainly, the commercial generation of H<sub>2</sub>O<sub>2</sub> follows the anthraquinone process, which includes two steps: the conversion of 2-alkyl-anthraquinone to alkyl-anthraquinone followed by high-energy oxidation and hydrogenation processes using noble-metal-based catalysts in organic solvents. As the anthraquinone process involves multiple steps and is an energy-consuming method, it is applicable only for large-scale production, and is thus considered as an environmentally unfriendly approach. To overcome this, there



has been growing research interest in the production of  $H_2O_2$  through photocatalysis. This process mainly involves water, oxygen, semiconductors, and sunlight, and is therefore considered a green pathway. However, typically, the photocatalytic production of  $H_2O_2$  gives low yields owing to the photocatalysts' poor visible light absorption, rapid recombination of excitons, and limited surface active sites.<sup>3–6</sup>

Additionally, the photon-assisted hydrogen evolution reaction *via* water splitting has been carried out to estimate the photocatalytic characteristics of semiconducting materials. The generation of  $H_2$  from the photocatalytic water splitting reaction has become an emerging research topic since the discovery by Fujishima and Honda's hydrogen production from  $H_2O$  using a  $TiO_2$  semiconductor under light irradiation, with the aim of reducing the world's reliance on fossil fuels for energy.<sup>7–10</sup> Moreover, the construction of a cost-effective, sustainable, and environmentally friendly photocatalytic semiconductor that is capable of performing this reaction has received much interest from the scientific community and remains a grand challenge.<sup>11</sup> Amongst the various semiconducting materials, MOFs are receiving a lot of attention owing to their exceptional characteristics, including ultra-high surface area, tuneable porosity, easy fabrication, flexible functionality, and large numbers of surface active sites. MOFs are 3D porous coordination polymers containing metal nodes/clusters that are connected with the organic linkers through coordination bonds.<sup>12,13</sup> They are promising for use as photocatalysts owing to their superior light-harvesting capacity, band structure tuneability, and populous active sites. Moreover, these exceptional features boost the potential for MOFs to be used as an efficient material for several other applications, such as chemical sensing, wastewater treatment, drug delivery, and organic pollutant degradation. From the perspective of band structure, the metal centre's vacant outside orbitals contribute mostly to the valence band (VB), whereas the outer orbitals of the organic linkers contribute primarily to the conduction band (CB) of the MOF.<sup>14,15</sup> Ligand to metal/cluster charge transfer, also known as LCCT or LMCT, is the process through which the linker efficiently captivates sunlight and transmits energy to the metal centre. Additionally, MOFs demonstrate the two essential conditions for a water redox reaction of a proper band gap accompanied by a tolerable band edge potential and they also exhibit long-term stability against photocorrosion in aqueous solution. Among the largest family of MOFs, Zr-based MOFs such as the UiO-66 series are considered as highly stable and active materials towards various photocatalytic applications. Remarkably, the physicochemical characteristics of (Zr) UiO-66 allow them to be functionalized using substituted terephthalate linkers, such as  $-NH_2$ ,  $-Br$ , and  $-NO_2$ .<sup>16–18</sup> Thanks to these unique properties, the (Zr) UiO-66 series MOFs (UiO-66-NH<sub>2</sub>) can be used to photocatalyze the  $H_2$  and  $H_2O_2$  production reactions. However, the pristine UiO-66-NH<sub>2</sub> MOF suffers from rapid photogenerated exciton recombination, which prevents it from becoming an efficient photocatalyst. Hence researchers have followed various strategies to improve the exciton lifetime as well as light responsiveness of the pristine UiO-66-NH<sub>2</sub>.

MOFs. Typically, these strategies involve forming a heterojunction with suitable photocatalysts, post-synthetic modification of the framework, hetero metal atom doping, and metallic nanoparticle-based co-catalyst addition. Amidst several approaches, the addition of suitable metal nanoparticles as a co-catalyst significantly improves the photocatalytic characteristics of pristine Zr-MOFs. In recent years, bimetallic nanoparticles have captured massive attention in various research fields, including sensing, plasmonics, electrocatalysis, photocatalysis, and specifically heterogeneous catalysis.<sup>19–22</sup> As a new class of materials, bimetallic NPs are made up of two separate metal components. Typically, they display an amalgam of the qualities of the two component metals, thus making them superior to the individual metal components. Additionally, the physicochemical properties of bimetallic NPs can be improved through synergistic effects, such as lattice strain, electron effect, ensemble effect, and bifunctional effect. Particular attention has been focused on bimetallic cocatalysts using noble metals like Au–Ag, Ag–Pd or Au–Pd because bimetallic materials created using plasmonic materials can be useful as both charge collectors and light absorbers, thus simultaneously improving the photocatalytic performance. Hence, pristine MOFs with low photocatalytic yields demonstrate improved performance upon the addition of noble bimetallic NPs.<sup>23–26</sup>

Incorporation of metal nanoparticles into MOF frameworks has received massive attention in both catalysis and photocatalysis. Typically, zirconium(IV)-based MOF UiO-66-NH<sub>2</sub> has drawn a lot of interest recently because of its distinctive qualities, including light harvesting, high thermal and chemical stability, variable pore sizes, large specific surface area, and the potential for functionalization.<sup>27,28</sup> Amongst various noble metals, Ag nanoparticles are of interest due to the LSPR effect. Through coordination or electrostatic contact with the  $-NH_2$  groups in the MOF, Ag and Pd can be immobilised on the UiO-66-NH<sub>2</sub> surface *via* adsorption–reduction method. The benefits of incorporating metallic Ag and Pd include an increase in light-harvesting capacity as well as the ability to control the Schottky barrier height by varying the Ag:Pd molar ratio. In this work, Ag/Pd bimetallic NP-loaded MOF nanocomposites are studied for photocatalytic  $H_2O_2$  and  $H_2$  production, giving significantly superior yield to that of the pristine MOF (UiO-66-NH<sub>2</sub>).<sup>23,29</sup>

## 2. Materials and methods

### 2.1. Chemicals used

Zirconium chloride ( $ZrCl_4$ ), sodium tetrachloropalladate ( $Na_2PdCl_4$ ), 2-amino-1,4-benzene dicarboxylic acid (BDC-NH<sub>2</sub>), silver nitrate ( $AgNO_3$ ), sodium borohydride ( $NaBH_4$ ), and Nafion-117 were purchased from Sigma-Aldrich. Sodium sulphate ( $Na_2SO_4$ ), *N,N*-dimethyl formamide (DMF), potassium bromide (KBr), methanol (MeOH), and isopropanol (IPA) were acquired from Merck and used without any additional



refinement. For all reactions carried out in this study deionized water was used.

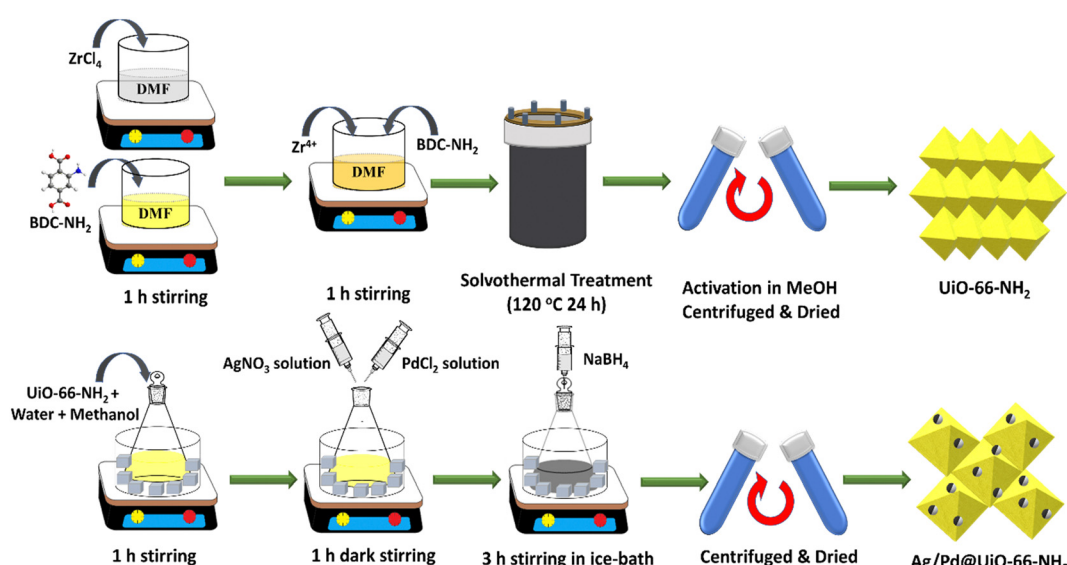
**2.1.1. Fabrication of  $\text{UiO-66-NH}_2$ .** The fabrication of  $\text{UiO-66-NH}_2$  was carried out according to a previously reported facile solvothermal approach.<sup>18,30</sup> The synthesis process includes the separate stirring of 2-aminoterephthalic acid (0.38 g, 2 mmol) and zirconium chloride (0.47 g, 2 mmol) for 60 min in DMF as the solvent (40 mL each). The two prepared solutions were then added together and the mixture was again subjected to stirring for 60 minutes. Thereafter, the resultant solution was subjected to solvothermal treatment in a Teflon-lined autoclave (24 h/120 °C). The autoclave was subjected to gradual cooling at room temperature and then solvent exchange was done using methanol to remove the unreacted metal salt/organic parts, followed by drying in an oven (24 h/70 °C). Finally, the prepared yellow-coloured material was ground and termed as  $\text{UiO-66-NH}_2$ .

**2.1.2. Fabrication of  $\text{Ag@UiO-66-NH}_2$ ,  $\text{Pd@UiO-66-NH}_2$ , and  $\text{Ag/Pd@UiO-66-NH}_2$ .** By following the adsorption-reduction procedure, bimetallic (Ag and Pd) nanoparticle-decorated  $\text{UiO-66-NH}_2$  was fabricated.<sup>29,31</sup> In the typical process, 0.3 g of pristine  $\text{UiO-66-NH}_2$  was introduced to 50 mL of water/methanol solution (1:1, v/v) followed by continuous stirring for 1 h. Then, to this solution the Ag and Pd salts were introduced followed by dropwise addition of  $\text{NaBH}_4$  solution at low temperature (in an ice bath). Five separate  $\text{UiO-66-NH}_2$  solutions were arranged followed by the addition of 0.025 M of  $\text{AgNO}_3$  (7 mL), 0.025 M  $\text{PdCl}_2$  (7 mL),  $\text{AgNO}_3 + \text{PdCl}_2$  (2.4 + 4.6 mL, 0.025 M),  $\text{AgNO}_3 + \text{PdCl}_2$  (3.5 + 3.5 mL, 0.025 M), or  $\text{AgNO}_3 + \text{PdCl}_2$  (4.6 + 2.4 mL, 0.025 M) solutions separately in five different reaction bottles. Stirring was carried out at low temperature for 1 h followed by the dropwise addition of 5 mL of  $\text{NaBH}_4$  (0.05 M) to each reaction solution for the reduction of adsorbed  $\text{AgNO}_3$  or/and  $\text{PdCl}_2$ . This reaction was carried out for 3 h and then the obtained suspension was

centrifuged and dried in an oven at 70 °C overnight. The dried samples were labelled as  $\text{Ag@UiO-66-NH}_2$ ,  $\text{Pd@UiO-66-NH}_2$ , (1:1)  $\text{Ag/Pd@UiO-66-NH}_2$ , (1:2)  $\text{Ag/Pd@UiO-66-NH}_2$ , and (2:1)  $\text{Ag/Pd@UiO-66-NH}_2$ , respectively. The typical synthesis procedure for  $\text{UiO-66-NH}_2$  and  $\text{Ag/Pd@UiO-66-NH}_2$  is illustrated in Scheme 1. The details of the characterization techniques used and additional experimental procedures followed in this work are discussed in the ESI† (1. Experimental techniques).

**2.1.3. Photocatalytic  $\text{H}_2\text{O}_2$  and  $\text{H}_2$  production.** The photocatalytic performance of the synthesized samples towards  $\text{H}_2\text{O}_2$  production was tested in an  $\text{O}_2$  atmosphere under visible light illumination for 2 h ( $\lambda > 420$  nm). A solution of 19 mL of deionized water (DI) and 1 mL of isopropanol (IPA) was mixed with 20 mg of the synthesized material. The mixture was then ultrasonicated for 10 min to completely disperse the contents. Thereafter, the resulting solution was purged with  $\text{O}_2$  for 30 min to obtain an  $\text{O}_2$ -saturated environment, followed by light irradiation. When the reaction time was over, the suspended solution was centrifuged to obtain a clear solution. Then, 1 mL of the resultant solution was taken, to which 0.1 M KI solution (2 mL) and 0.01 M ammonium molybdate solution (0.05 mL) were added to develop a light-yellow colour in the liquid sample. Finally, the concentration of photocatalytically produced  $\text{H}_2\text{O}_2$  was evaluated using a UV-visible spectrophotometer.

Additionally, the photocatalytic  $\text{H}_2$  evolution ability of the synthesized photocatalysts was further studied. Herein, a 100 mL sealed quartz batch reactor was used to investigate the photocatalytic  $\text{H}_2$  production capacity of the fabricated pristine  $\text{UiO-66-NH}_2$  and  $\text{Ag@UiO-66-NH}_2$ ,  $\text{Pd@UiO-66-NH}_2$  and  $\text{Ag/Pd@UiO-66-NH}_2$  composites. The produced nanomaterials (20 mg) were introduced into 20 mL of 10% MeOH-water solution and placed in the photoreactor. A xenon arc lamp (300 W,  $\lambda \geq 420$  nm) was used as the visible light source and was illuminated for 1 h. The reactor's contents were stirred thoroughly to



Scheme 1 Schematic representation of the preparation of  $\text{UiO-66-NH}_2$  and  $\text{Ag/Pd@UiO-66-NH}_2$ .



avoid particle aggregation and promote uniform distribution throughout the reaction medium. Prior to placing under the Xe lamp, the solution was rigorously purged with bubbling  $\text{N}_2$  gas for 30 minutes to eliminate dissolved gases. The evolved gaseous compounds were collected using direct water displacement and analysed using gas chromatography (GC; GC-7890B, Agilent Technologies) customised with 5  $\text{\AA}$  molecular sieves and a thermal conductivity detector (TCD).

### 3. Physicochemical characterization

#### 3.1. Structural characterization

The crystallographic structure and nature of the MOF-based composite materials was studied through X-ray diffraction (XRD) method. The resulting diffraction patterns for pristine  $\text{UiO-66-NH}_2$ ,  $\text{Ag@UiO-66-NH}_2$ ,  $\text{Pd@UiO-66-NH}_2$  and the  $\text{UiO-66-NH}_2$  nanocomposites decorated with different ratios of Ag: Pd (1:1, 1:2, and 2:1 Ag/Pd@ $\text{UiO-66-NH}_2$ ) are displayed in Fig. 1(a). The intense peak exhibits the outstanding crystallinity of neat  $\text{UiO-66-NH}_2$ , which is similar to previous reports.<sup>32</sup> The diffraction pattern remained analogous even after adding Ag and Pd to the parent  $\text{UiO-66-NH}_2$  by following the adsorption-reduction process, demonstrating the unchanged rigid framework of the MOF in the composites. Additionally, the peak intensity of  $\text{UiO-66-NH}_2$  is slightly reduced in the synthesized composite materials, which might be due to robust interaction between the MOF and the loaded noble metal nanoparticles.<sup>29</sup> However, a small peak was observed at  $2\theta = 46.3^\circ$  in the  $\text{Ag@UiO-66-NH}_2$  and  $\text{Ag/Pd@UiO-66-NH}_2$  composites, which corresponds to the (200) crystal plane of Ag.<sup>33–35</sup> The Pd NPs decorated in  $\text{Pd@UiO-66-NH}_2$  and  $\text{Ag/Pd@UiO-66-NH}_2$  did not exhibit any additional diffraction peaks owing to their low weight percentage and the possibility that the diffraction peaks of the Pd metallic nanoparticles might merge with those of the  $\text{UiO-66-NH}_2$ .<sup>36</sup> Moreover, the existence of both Ag and Pd NPs in the composite was further supported by XPS, electron microscopy, colour mapping, and EDAX analysis results.

To confirm the various functional groups present in  $\text{UiO-66-NH}_2$  and the prepared Ag and Pd nanocomposites, an FTIR study was performed and the outcomes are shown in Fig. 1(b). A double peak was observed for pristine  $\text{UiO-66-NH}_2$  at 3340 and 3477  $\text{cm}^{-1}$ , which are the symmetric and asymmetric stretching frequencies for  $-\text{NH}_2$  groups, respectively. Two peaks were seen in the lower wavenumber area, at 1642  $\text{cm}^{-1}$  and 1244  $\text{cm}^{-1}$ , which correspond to the distinctive bending vibration of N-H and the stretching vibration for C-N of aromatic amines, respectively.<sup>32</sup> In addition, the smaller vibrational band at 1510  $\text{cm}^{-1}$  denotes the C=C vibration of the benzene ring.<sup>28</sup> Furthermore, the peaks observed for the vibrational frequency at the lower range, *i.e.*, around 481, 661, and 776  $\text{cm}^{-1}$ , are connected to the asymmetric stretching of metal-(OC), O=C=O bending, and C=C stretching vibrations, respectively. FTIR analysis of the Ag- and/or Pd-nanoparticle-loaded composites exhibited an analogous pattern to that of the parent Zr-MOF, suggesting indistinguishable chemical bonding environments and functional groups present in the framework structure. This observation further corroborates the retention of the framework of  $\text{UiO-66-NH}_2$  after noble bimetallic nanoparticle loading, as earlier seen from XRD analysis. The aforementioned FTIR spectra exhibited good concordance with the outcomes described in the literature.<sup>18,27,28</sup>

The surface area (BET) and pore size (BJH) distribution of (1:2) Ag/Pd@ $\text{UiO-66-NH}_2$  were studied using the  $\text{N}_2$  adsorption-desorption isotherm technique. The plot of the results exhibited that a typical type-I isotherm was followed, which confirms the microporous and mesoporous nature of the obtained composite material, as depicted in Fig. S2 (ESI†). Furthermore, after the surface modification of the MOF with the noble metal NPs, the isotherm pattern remains unchanged but a decrease in surface area was observed as depicted in Fig. S1 (ESI†). This lowering of surface area ( $\text{UiO-66-NH}_2 = 831.49 \text{ m}^2 \text{ g}^{-1}$ ,<sup>32</sup> (1:2) Ag/Pd@ $\text{UiO-66-NH}_2 = 681.29 \text{ m}^2 \text{ g}^{-1}$ ) is based on the metal nanoparticle loading on the MOF surface. In short, the deposition of Ag/Pd bimetallic NPs on the  $\text{UiO-66-NH}_2$  surface or the presence of trapped recrystallized BDC- $\text{NH}_2$

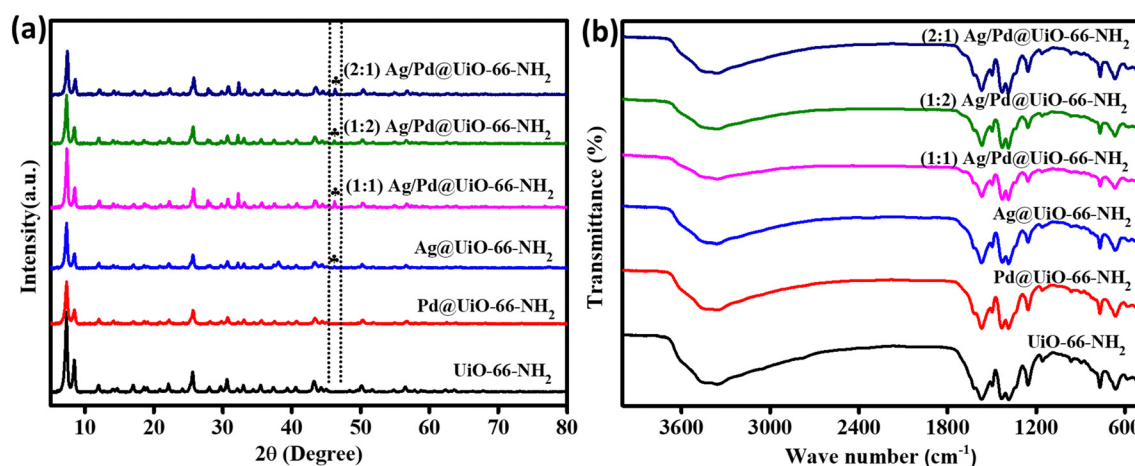


Fig. 1 (a) XRD patterns and (b) FTIR spectra for  $\text{UiO-66-NH}_2$ ,  $\text{Ag@UiO-66-NH}_2$ ,  $\text{Pd@UiO-66-NH}_2$ , and (1:1, 1:2, 2:1) Ag/Pd@ $\text{UiO-66-NH}_2$ .



moieties in the  $\text{UiO-66-NH}_2$  pores may be the cause of the reduction in surface area of (1:2)  $\text{Ag/Pd@UiO-66-NH}_2$  compared with  $\text{UiO-66-NH}_2$ .<sup>17,31,36</sup> The pore volume distribution for the composite (1:2)  $\text{Ag/Pd@UiO-66-NH}_2$  exhibits a micro-porous nature that is similar to the parent  $\text{UiO-66-NH}_2$ .

X-ray photoelectron spectroscopy (XPS) is used to determine the oxidation states of various elements present in materials. Thus, XPS analysis was carried out to elucidate the electronic valence states of several elements, such as C, N, Zr, O, Ag, and Pd, in the prepared composite materials. Fig. S2 (ESI†) shows the XPS survey spectra for the pristine  $\text{UiO-66-NH}_2$  and the composite (1:2)  $\text{Ag/Pd@UiO-66-NH}_2$ , which supports the presence of N 1s, O 1s, C 1s, and Zr 3d in pristine  $\text{UiO-66-NH}_2$  and C 1s, N 1s, O 1s, Zr 3d, Ag 3d, and Pd 3d in the composite (1:2)  $\text{Ag/Pd@UiO-66-NH}_2$ . The obtained deconvoluted peaks for  $\text{UiO-66-NH}_2$  were located at 284.99, 286.30, and 288.96 eV in the C 1s spectrum, which corresponds to the  $\text{C}=\text{C}$ ,  $\text{C}-\text{NH}_2$ , and  $\text{O}=\text{C}-\text{O}$  of the linker, respectively. The N 1s spectrum for the pristine MOF was deconvoluted into peaks at 399.52, 400.63, and 401.76 eV for the  $-\text{NH}_2$ ,  $-\text{NH}_3^+$ , and  $=\text{NH}_2^+$  groups of the linker, respectively. The O 1s peak was observed at 532.14 eV, which represents the Zr–O bond, and the Zr 3d spectrum was deconvoluted to give the Zr 3d<sub>5/2</sub> and Zr 3d<sub>3/2</sub> peaks at 183.13 and 185.61 eV, respectively, as depicted in

Table 1.<sup>18</sup> Afterwards, the obtained deconvoluted peaks for the bimetallic (Ag/Pd)-modified  $\text{UiO-66-NH}_2$  were positioned at 284.78, 286.2, and 288.75 eV corresponding to  $\text{C}=\text{C}$ ,  $\text{C}-\text{NH}_2$ , and  $\text{O}=\text{C}-\text{O}$  for C 1s, which shows slight variation from the pristine material. The N 1s spectrum of (Ag/Pd)-modified  $\text{UiO-66-NH}_2$  shows deconvoluted peaks at 399.37, 400.51, and 401.23 eV which represent the  $-\text{NH}_2$ ,  $-\text{NH}_3^+$ , and  $=\text{NH}_2^+$  groups of the linker, respectively. For O 1s, the peaks were obtained at 530.25, 531.84, and 532.63 eV, which correspond to lattice oxygen, Zr–O, and surface-adsorbed  $\text{H}_2\text{O}$ , respectively. For Zr 3d, the peaks deconvoluted into 183.01 eV and 185.39 eV, associated with Zr 3d<sub>5/2</sub> and Zr 3d<sub>3/2</sub>, respectively, with slight shifting relative to the peaks for pristine  $\text{UiO-66-NH}_2$ , as explained in Table 1. In the as-synthesized composite photocatalyst, the oxidation states of the noble metals Ag and Pd were deconvoluted into two peaks because of spin-orbit coupling. The deconvoluted peaks for Ag in (1:2)  $\text{Ag/Pd@UiO-66-NH}_2$  were obtained at 368.26 and 374.28 eV for the 3d<sub>3/2</sub> and 3d<sub>5/2</sub> spin states, respectively. In contrast, the Pd spectrum was deconvoluted into 335.5 and 339.2 eV, representing 3d<sub>5/2</sub> and 3d<sub>3/2</sub>, respectively, in the (1:2)  $\text{Ag/Pd@UiO-66-NH}_2$  composite. These obtained oxidation states of Ag and Pd validate the successful preparation of bimetallic Ag(0) and Pd(0) species from the reduction of

Table 1 XPS data for the prepared materials

	Binding energy in eV			Ref.
Element	Carbon/C 1s			
$\text{UiO-66-NH}_2$	284.99	286.30	288.96	32 and 35
Ag/Pd@ $\text{UiO-66-NH}_2$	284.78	286.21	288.75	
Speculation:	$\text{C}=\text{C}$ of linker	$\text{C}-\text{NH}_2$ of linker	( $\text{O}=\text{C}-\text{O}$ ) of linker	
Difference:	−0.21	−0.09	−0.21	
Element	Nitrogen/N 1s			
$\text{UiO-66-NH}_2$	399.52	400.63	401.76	18 and 37
Ag/Pd@ $\text{UiO-66-NH}_2$	399.37	400.51	401.23	
Speculation:	$-\text{NH}_2$ of linker	$-\text{NH}_3^+$ of linker	$=\text{NH}_2^+$ of linker	
Difference:	−0.15	−0.12	−0.53	
Element	Oxygen/O 1s			
$\text{UiO-66-NH}_2$	—	532.14	—	27 and 29
Ag/Pd@ $\text{UiO-66-NH}_2$	530.25	531.84	532.63	
Speculation:	Lattice O	Zr–O bond	Adsorbed $\text{H}_2\text{O}$	
Difference:		−0.30	—	
Element	Zirconium/Zr 3d			
$\text{UiO-66-NH}_2$	183.13		185.61	28 and 29
Ag/Pd@ $\text{UiO-66-NH}_2$	183.01		185.39	
Speculation:	$\text{Zr}^{4+}$ (3d <sub>5/2</sub> )		$\text{Zr}^{4+}$ (3d <sub>3/2</sub> )	
Difference:	−0.12		−0.22	
Element	Silver/Ag 3d			
$\text{UiO-66-NH}_2$	—		—	38–40
Ag/Pd@ $\text{UiO-66-NH}_2$	368.26		374.28	
Speculation:	Ag (3d <sub>5/2</sub> )		Ag (3d <sub>3/2</sub> )	
Difference:	—		—	
Element	Palladium/Pd 3d			
$\text{UiO-66-NH}_2$	—		—	31, 33 and 37
Ag/Pd@ $\text{UiO-66-NH}_2$	335.50		339.20	
Speculation:	Pd (3d <sub>5/2</sub> )		Pd (3d <sub>3/2</sub> )	
Difference:	—		—	



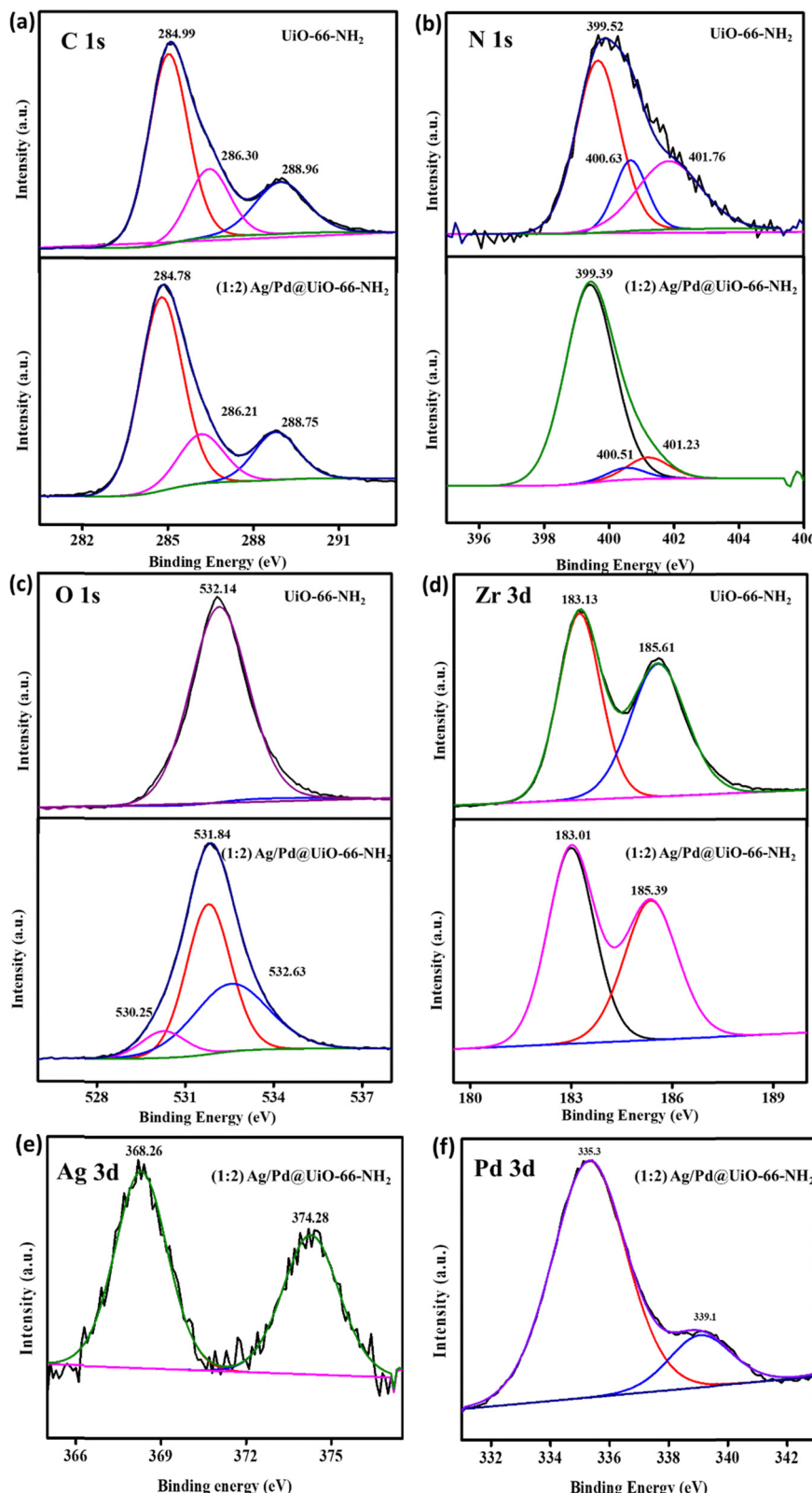


Fig. 2 (a) C 1s, (b) N 1s, (c) O 1s, (d) Zr 3d, (e) Ag 3d, and (f) Pd 3d XPS spectra for  $\text{UiO-66-NH}_2$  and the (1:2) Ag/Pd@ $\text{UiO-66-NH}_2$  composite.

$\text{AgNO}_3^-$  and  $\text{PdCl}_2^-$  ions, respectively. The existence of Ag/Pd in the MOF composite was confirmed by XPS and further

corroborated by the EDS, elemental mapping, and TEM results (Fig. 2).

### 3.2. Morphological characterization

The morphology of the synthesized photocatalysts was characterized through FESEM and HRTEM. The clustered morphology of the composite is clearly exhibited in the FESEM image of (1 : 2) Ag/Pd@UiO-66-NH<sub>2</sub>. Furthermore, the HRTEM image of (1 : 2) Ag/Pd@UiO-66-NH<sub>2</sub> exhibits the deposition of Ag/Pd on the surface of UiO-66-NH<sub>2</sub>, which can be seen as black spots on the MOF structure.<sup>39,41</sup> The lattice fringe of the parent MOF could not be clearly observed due to the sensitivity of the UiO-66-NH<sub>2</sub> framework towards the electron beam bombardment, but the lattice fringe was observed for (1 : 2) Ag/Pd@UiO-66-NH<sub>2</sub> at 0.24 and 0.22 nm, which corresponds to Ag and Pd nanoparticles and shows good agreement with the (111) plane of Ag and (111) plane of Pd in the bimetallic nanoparticles,

respectively.<sup>34,37</sup> Moreover, the HRTEM analysis suggests that the bimetallic Ag/Pd NPs present in the composite have spherical morphology. The colour mapping and EDAX results for the (1 : 2) Ag/Pd@UiO-66-NH<sub>2</sub> composite are presented in Fig. 3(e)–(k), confirming the existence of C, N, O, Zr, Ag, and Pd, respectively. Moreover, the uniform distribution of Ag/Pd on the MOF can be seen from the elemental mapping results.

### 3.3. Optical and electrochemical characterization

To study the optical properties of the prepared photocatalyst materials, specifically the parent UiO-66-NH<sub>2</sub> and the bimetallic nanoparticle-loaded composites, UV-Vis diffuse reflectance (UV-DRS) investigation was performed, as shown in Fig. 4(a). From the DRS spectra, the neat UiO-66-NH<sub>2</sub> exhibits two acute

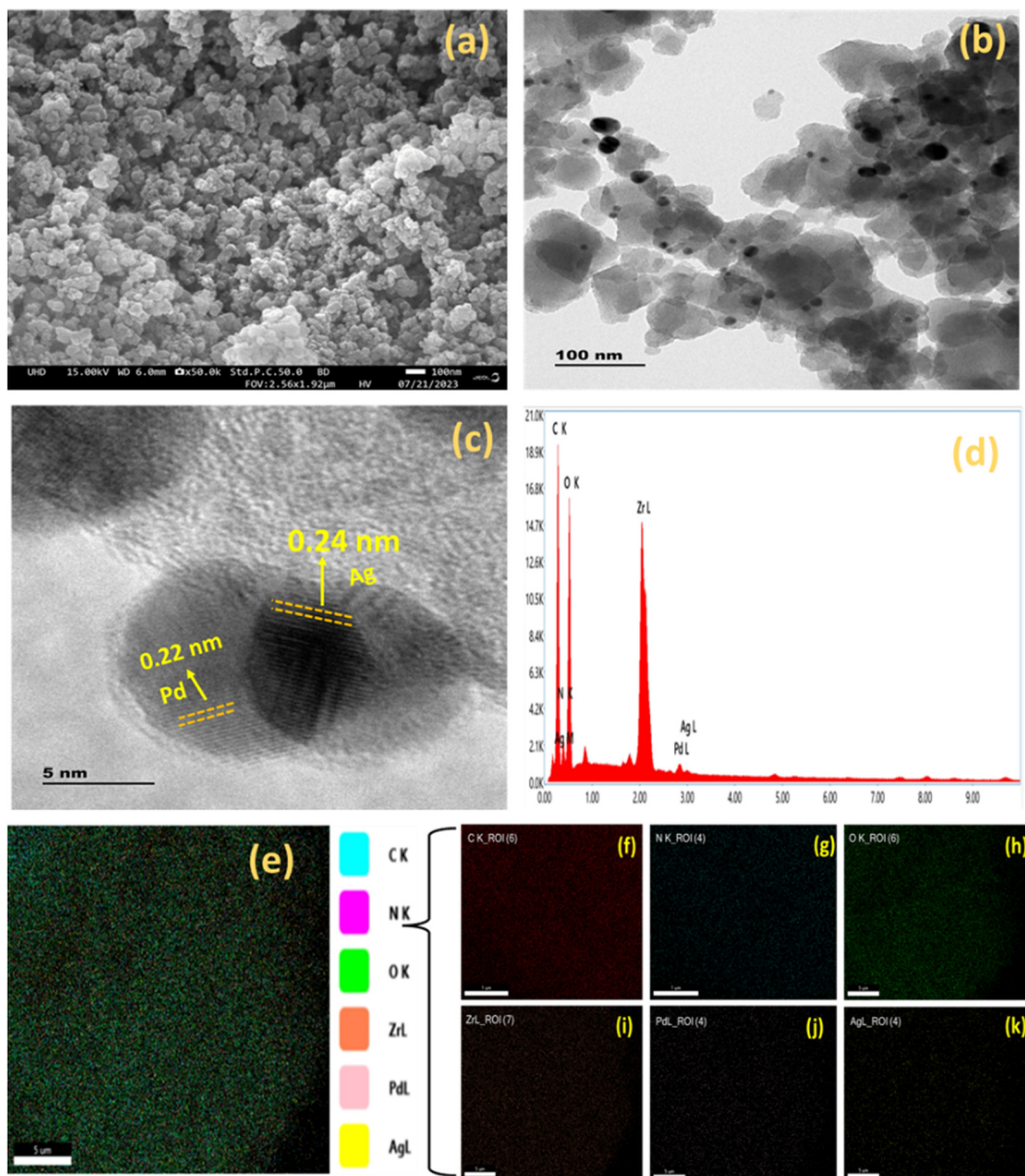


Fig. 3 (a) FESEM image of Ag/Pd@UiO-66-NH<sub>2</sub>, (b) HRTEM image of Ag/Pd@UiO-66-NH<sub>2</sub>, (c) HRTEM image showing lattice fringes of Ag/Pd@UiO-66-NH<sub>2</sub>, (d) EDAX results for Ag/Pd@UiO-66-NH<sub>2</sub>, and (e)–(k) elemental colour mapping results for Ag/Pd@UiO-66-NH<sub>2</sub>.



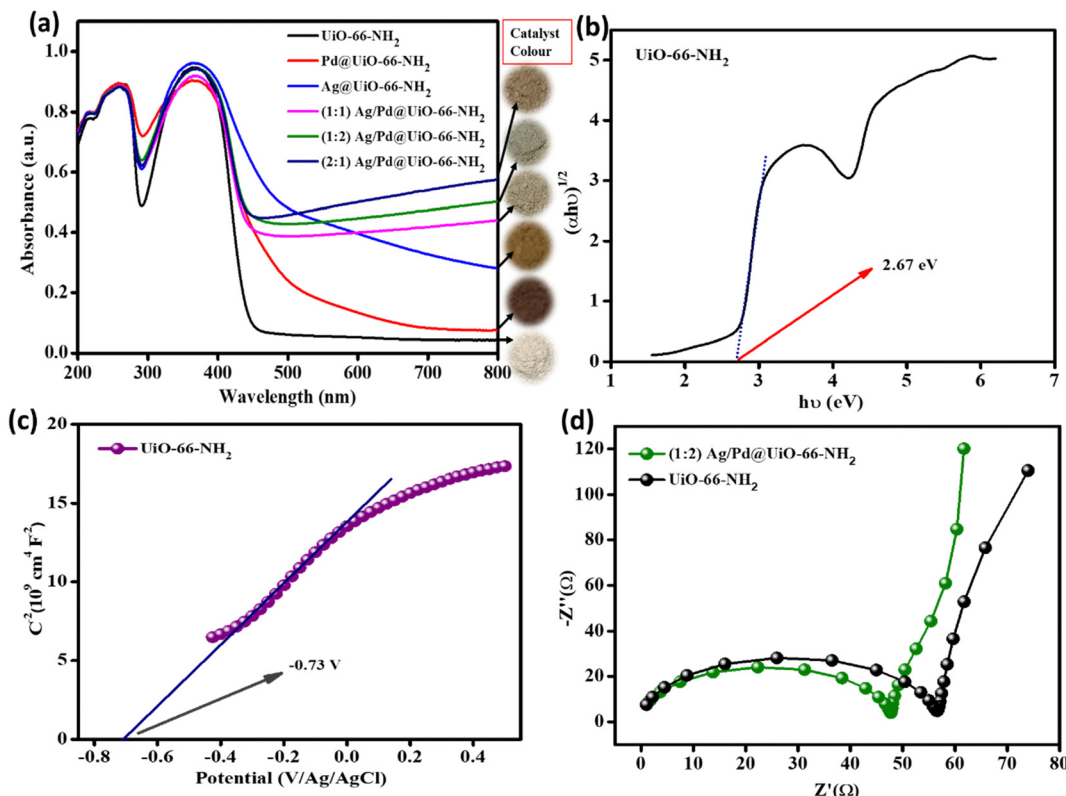


Fig. 4 (a) UV-Vis DRS spectra for the prepared samples. (b) Tauc plot for  $\text{UiO-66-NH}_2$ , (c) MS plot for parent  $\text{UiO-66-NH}_2$ , and (d) EIS plots for  $\text{UiO-66-NH}_2$  and  $(1:2) \text{Ag/Pd@UiO-66-NH}_2$ .

bands at around 265 and 370 nm, which can be attributed to the  $n-\pi^*$  transition of the lone pair of electrons of the  $-\text{NH}_2$  group of the linker and the  $\pi-\pi^*$  transition of the ATA linker with the Zr-oxy cluster absorption, respectively. Likewise, analogous bands to those of the parent  $\text{UiO-66-NH}_2$  were observed for the bimetal-loaded composites, as shown in Fig. 4(a).<sup>18,28</sup> However, the bimetal loading was accompanied with gradual red shifting, which signifies the more robust photon receptiveness of the composite MOFs upon the varied addition of Ag/Pd. Moreover, the deposition of metal nanoparticles led to substantial absorption beginning at 800 nm and extending into the intrinsic  $\text{UiO-66-NH}_2$  absorption bands because of localised surface plasmon resonance (LSPR) as well as the d-d transitions of both the noble metals. Compared with individual metal deposition (Ag or Pd), this effect was significantly more noticeable in the Ag/Pd bimetallic nanoparticle-loaded MOF composites. Ag nanoparticles often exhibit a distinctive LSPR peak between 410 and 480 nm, but depending on the size, shape, and refractive index of the surrounding medium, its wavelength can vary throughout a wide range. In the current study, no strong LSPR peak was observed for Ag NPs, which is due to the small particle size and uniform dispersion of the Ag NPs,<sup>34</sup> which results in the strong absorption of the MOF composites. Pd metal exhibits strong absorbance up to 650 nm in the visible light range. The LSPR effect was not seen for the (1:1, 1:2, and 2:1) Ag/Pd@ $\text{UiO-66-NH}_2$  composites, but the region was intensified and made wider by the Pd metal presence in

the Ag/Pd-modified  $\text{UiO-66-NH}_2$ .<sup>34</sup> So, by loading both the metals, strong visible light absorbance occurred owing to positive synergism amongst the metal nanoparticles and the MOF support. The absorption of visible light by the Ag/Pd nanoparticle-loaded MOF is considerably stronger than that of the Pd- or Ag- loaded  $\text{UiO-66-NH}_2$  individually, demonstrating the creation of superior light-responsive bimetallic nanoparticles with respect to monometallic particles. Moreover, the material underwent an indirect transition, and for the parent  $\text{UiO-66-NH}_2$  MOF the optical band gap obtained from the Tauc plot was around 2.67 eV, as shown Fig. 4(b), and the band gaps of all of the noble metal-loaded  $\text{UiO-66-NH}_2$  are reduced with respect to the pristine material. So, the above results demonstrated that the loading of Ag/Pd nanoparticles improved the light-harvesting tendency compared to the monometallic or pristine MOF counterparts. By following Kubelka-Munk equation (eqn (1)), the band gap of  $\text{UiO-66-NH}_2$  was obtained.

$$\alpha h\nu = A(h\nu - E_g)^{n/2} \quad (1)$$

The respective band edge potential of the so-formed MOF was evaluated by UV-Vis investigation and following eqn (2):

$$E_g = \text{VB} - \text{CB} \quad (2)$$

Furthermore, PL analysis was performed for the prepared pristine MOF and the Ag/Pd-loaded MOF-based photocatalysts. The PL study gives clear evidence of the separation and



recombination of the photogenerated exciton pairs, as depicted in Fig. S3 (ESI<sup>†</sup>).<sup>42</sup> The peak intensity is indirectly associated with the exciton separation efficacy, *i.e.*, high intensity peaks mean a higher exciton recombination rate and low intensity peaks indicate a minimal recombination rate. From the plotted PL analysis peaks, it has been revealed that the (1:2) Ag/Pd@UiO-66-NH<sub>2</sub> composite exhibits a higher life span of photogenerated e<sup>-</sup> and h<sup>+</sup> than those of the pristine UiO-66-NH<sub>2</sub> and other composites.<sup>29,39</sup> The aforementioned results are clearly supported by EIS measurements. Additionally, through time-resolved photoluminescence (TRPL) analysis technique, the lifespans of the photoexcited electrons of UiO-66-NH<sub>2</sub> and (1:2) Ag/Pd@UiO-66-NH<sub>2</sub> were obtained, as depicted in Fig. S4 (ESI<sup>†</sup>), which was fitted using a model biexponential eqn (3):

$$R(t) = A_1 \exp\{-t/\tau_1\} + A_2 \exp\{-t/\tau_2\} \quad (3)$$

Here,  $R$  denotes the normalized emission intensity,  $\tau$  signifies the lifetime of photogenerated excitons for each component,  $A$  is the amplitude, and  $t$  is the time left after pulsed laser excitation. The essential decay and the average lifetime ( $\tau_{\text{avg}}$ ) of two exponentials demonstrate the inclusive TRPL character, which can be calculated using eqn (4):

$$\tau_{\text{avg}} = \frac{A_1 \tau_1^2 + A_2 \tau_2^2}{A_1 \tau_1 + A_2 \tau_2} \quad (4)$$

where  $\tau_1$  and  $\tau_2$  represent the trapping period for electrons and exciton pair generation, respectively. The fluorescence lifetimes were obtained by fitting the decay profile in Table S1 (ESI<sup>†</sup>) with the biexponential terms. Hence, the average excited lifetimes of UiO-66-NH<sub>2</sub> and (1:2) Ag/Pd@UiO-66-NH<sub>2</sub> were found to be 0.504 ns and 0.537 ns, respectively (Table S1, ESI<sup>†</sup>). So, from the result it can be clearly seen that the average lifetime of (1:2) Ag/Pd@UiO-66-NH<sub>2</sub> is longer, which explains the lower exciton recombination rate, thereby boosting the photocatalytic activity.

Moreover, to understand the better exciton separation efficacy of the Ag/Pd@UiO-66-NH<sub>2</sub> composite as compared with the parent UiO-66-NH<sub>2</sub>, both the materials were studied by electrochemical impedance spectroscopy (EIS) under zero bias potential. In the Nyquist plots, the smaller arc radius in the high-frequency zone for the composite (1:2) Ag/Pd@UiO-66-NH<sub>2</sub> indicates a lower recombination rate of e<sup>-</sup>/h<sup>+</sup> pairs as compared to that of the pristine UiO-66-NH<sub>2</sub>. The aforementioned finding indicates that the process of charge migration in the composites was relatively smooth and the charge transfer resistance at the interface was noticeably low, which was the primary factor contributing to the composite's higher catalytic activity than that of neat UiO-66-NH<sub>2</sub> under identical experimental conditions, as depicted in Fig. 4(d). The EIS results further support the PL data and exhibit good correlation. In addition, current *versus* potential measurement (LSV) was carried out to study the transfer of photogenerated excitons and the photocatalytic mechanism. The analysis was performed for the parent UiO-66-NH<sub>2</sub>, and all the Ag- and/or Pd-loaded UiO-66-NH<sub>2</sub> composites at 5 mV s<sup>-1</sup> in a suitable potential

range, as shown in Fig. S5 (ESI<sup>†</sup>). The pristine UiO-66-NH<sub>2</sub> MOF produces an anodic photocurrent, which indicates n-type characteristics. Moreover, the Ag- and/or Pd-nanoparticle-loaded composites show similar properties, possessing improved photocurrent compared to that of the pristine MOF.

MS (Mott-Schottky) analysis of the neat UiO-66-NH<sub>2</sub><sup>18</sup> was performed to explain the band structure, the type of semiconductor material (p-type/n-type), and the flat band potential, as depicted in Fig. 4(c). The MS plot of pristine UiO-66-NH<sub>2</sub> shows a positive slope to the  $x$ -axis, which indicates the n-type nature of the parent UiO-66-NH<sub>2</sub>. The obtained flat band potential for the material is -0.73 V. The VB and CB positions calculated using eqn (5) were 2.03 eV and -0.64 eV, respectively, *versus* the NHE (at pH = 7).

$$E_{(\text{NHE}, \text{pH}=7)} = E_{\text{Ag}/\text{AgCl}} - 0.059 \times (7\text{-pH of the electrolyte}) + 0.198 \quad (5)$$

## 4. Photocatalytic performance

The photocatalytic efficiency of the prepared catalysts towards hydrogen peroxide (H<sub>2</sub>O<sub>2</sub>) and hydrogen (H<sub>2</sub>) production were analysed in this study. The production of H<sub>2</sub>O<sub>2</sub> in an O<sub>2</sub>-saturated atmosphere under irradiation of visible light ( $\lambda > 420$  nm) for 2 h at ambient conditions was thoroughly investigated. Moreover, in the absence of light or catalyst, no H<sub>2</sub>O<sub>2</sub> production was observed, which explains that light illumination and catalysts are the primary instigators for the reaction to take place. From Fig. 5(a), the H<sub>2</sub>O<sub>2</sub> production rate for UiO-66-NH<sub>2</sub> is 8.52  $\mu\text{mol h}^{-1}$ . Amongst the prepared composite materials, (1:2) Ag/Pd@UiO-66-NH<sub>2</sub> exhibits the highest photocatalytic H<sub>2</sub>O<sub>2</sub> production rate of 39.4  $\mu\text{mol h}^{-1}$ , as shown in Fig. 5(a). H<sub>2</sub>O<sub>2</sub> production rates of 18.6, 20.2, 37.3, and 34.8  $\mu\text{mol h}^{-1}$  were obtained for Ag@UiO-66-NH<sub>2</sub>, Pd@UiO-66-NH<sub>2</sub>, (1:1) Ag/Pd@UiO-66-NH<sub>2</sub>, and (2:1) Ag/Pd@UiO-66-NH<sub>2</sub>, respectively. As compared to the pristine UiO-66-NH<sub>2</sub>, the synthesized composite materials showed significantly enhanced H<sub>2</sub>O<sub>2</sub> production, which can be attributed to their superior light absorption capacity and lowering of the exciton pair recombination ability due to the presence of bimetallic Ag/Pd nanoparticles. The fabricated composite (1:2) Ag/Pd@UiO-66-NH<sub>2</sub> exhibits superior photocatalytic performance that is four-fold greater than that of the pristine UiO-66-NH<sub>2</sub> material. In addition, the reusability analysis of the composite materials showed that (1:2) Ag/Pd@UiO-66-NH<sub>2</sub> is photostable for up to four consecutive cycles, as illustrated in Fig. 5(b). Moreover, to study the O<sub>2</sub> dependency of the photocatalytic H<sub>2</sub>O<sub>2</sub> production by (1:2) Ag/Pd@UiO-66-NH<sub>2</sub>, the individual reactions were performed under Ar or O<sub>2</sub> gas purging, and only a small amount of H<sub>2</sub>O<sub>2</sub> was generated under the Ar atmosphere, as shown in Fig. 5(c). This suggests the dependence of the photocatalytic production of H<sub>2</sub>O<sub>2</sub> upon the presence of O<sub>2</sub>. Moreover, the effect of scavengers on the H<sub>2</sub>O<sub>2</sub> production is illustrated in Fig. 5(d) and discussed in detail in the subsequent



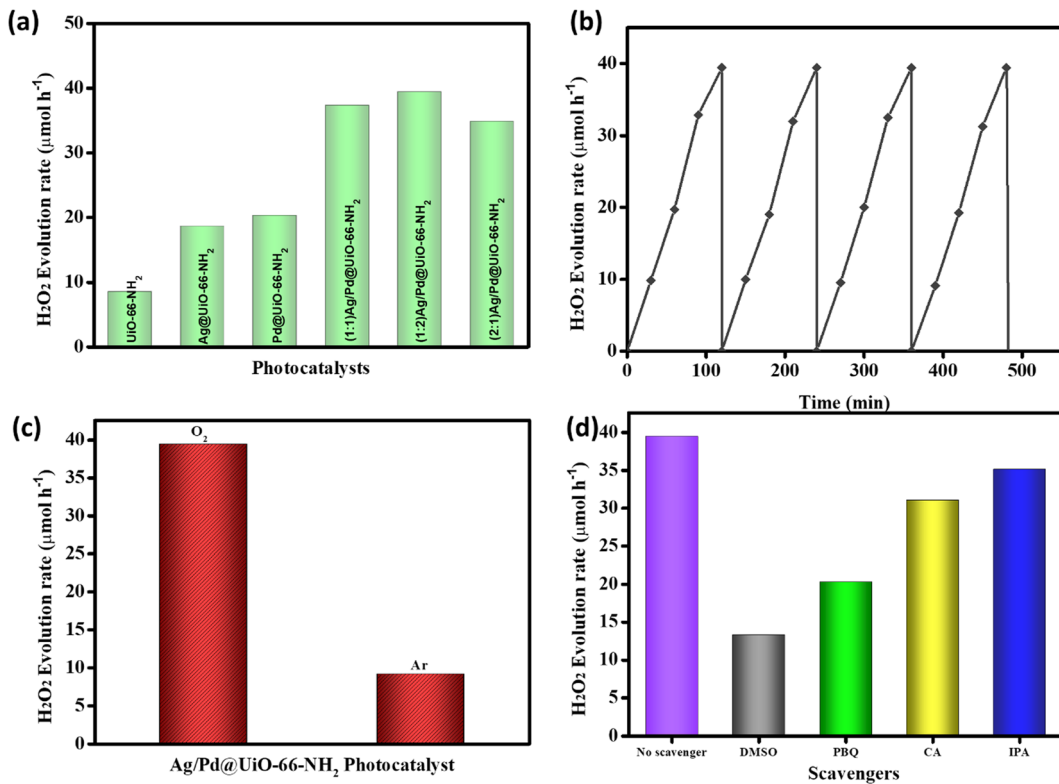


Fig. 5 (a) H<sub>2</sub>O<sub>2</sub> production rate of neat UiO-66-NH<sub>2</sub> and Ag- and/or Pd-loaded composites. (b) Reusability test for H<sub>2</sub>O<sub>2</sub> production over (1:2) Ag/Pd@UiO-66-NH<sub>2</sub> composite. (c) H<sub>2</sub>O<sub>2</sub> production rate in different environments. (d) Effect of scavengers on the H<sub>2</sub>O<sub>2</sub> production rate.

section. A comparison of the H<sub>2</sub>O<sub>2</sub> production rates is given in Table S3 (ESI<sup>†</sup>) to show the importance of the synthesized Ag/Pd@UiO-66-NH<sub>2</sub> composite.<sup>1,43</sup>

The photocatalytic efficacy of the synthesized samples was also measured through their H<sub>2</sub> evolution ability. The reaction was executed in a closed quartz batch reactor type with 100 mL volume, using 20 mg of catalyst in 20 mL of MeOH/water solution (10% v/v) at room temperature and atmospheric pressure. In the pre-irradiation stage, the reactor contents were stirred continuously to prevent the nanoparticles from settling with N<sub>2</sub> (gas) purging for 0.5 h to eliminate dissolved gases.

Thereafter, the light source was placed above the aqueous suspension at a distance of 8.7 cm from the bottom of the reactor. The samples were irradiated using a xenon arc lamp (300 W) with medium pressure as a source of visible light for 1 h. A GC-7890B (Agilent Technology) with 5 Å molecular sieves and a thermal conductivity detector was used to monitor the H<sub>2</sub> gas evolution. Blank readings were taken in the absence of a catalyst or light irradiation to prove that hydrogen evolution only occurs in the presence of both photocatalyst and light. The neat UiO-66-NH<sub>2</sub> exhibits a mere 115 μmol h<sup>-1</sup> of H<sub>2</sub> evolution because of the high recombination rate of the excitons.<sup>16</sup>

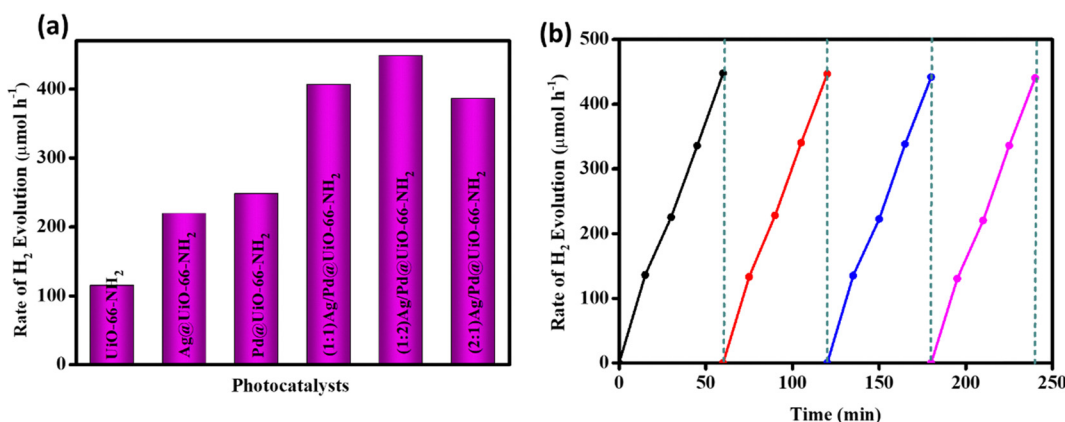


Fig. 6 (a) H<sub>2</sub> production rate of neat UiO-66-NH<sub>2</sub> and the Ag- and/or Pd-loaded composites. (b) Reusability test for H<sub>2</sub> production over the (1:2) Ag/Pd@UiO-66-NH<sub>2</sub> composite.

However, the Ag and/or Pd nanoparticle loading enhances the rate of  $H_2$  production due to the superior absorption of visible light accompanied with enhanced charge separation and transfer. The photocatalytic  $H_2$  evolution rates of the prepared composites  $Ag@UiO-66-NH_2$ ,  $Pd@UiO-66-NH_2$ , (1:1)  $Ag/Pd@UiO-66-NH_2$ , (1:2)  $Ag/Pd@UiO-66-NH_2$ , and (2:1)  $Ag/Pd@UiO-66-NH_2$  are 219.5, 248.1, 406.7, 448.2, and  $386.3 \mu\text{mol h}^{-1}$ , respectively, as shown in Fig. 6(a). From the resultant plot it was found that (1:2)  $Ag/Pd@UiO-66-NH_2$  shows the highest rate of photocatalytic  $H_2$  generation, which is four times greater than that of the pristine  $UiO-66-NH_2$ . The apparent conversion efficiency (ACE) is calculated to be 3.30%, as depicted in Table S2 (ESI†). The photostability of the (1:2)  $Ag/Pd@UiO-66-NH_2$  composite was confirmed by executing four successive cycles of  $H_2$  evolution, with no significant change in the production rate (Fig. 6(b)) or its post-photocatalytic XRD (Fig. S5, ESI†). Moreover, ICP-OES analysis of the spent (1:2)  $Ag/Pd@UiO-66-NH_2$  composite showed negligible change in the Ag–Pd loading percentage ( $Ag-Pd_{As-synthesized}$ : 1.4–2.4 wt% and  $Ag-Pd_{Post-use}$ : 1.25–2.26 wt%, respectively), suggesting the stability of the prepared photocatalyst. A comparison of the  $H_2$  evolution is given in Table S4 (ESI†) to show the importance of the prepared  $Ag/Pd@UiO-66-NH_2$  composite.

## 5. Mechanistic insights

The previously discussed analysis results involving physicochemical, morphological, and textural characteristics suggested the successful formation of bimetallic nanoparticle ( $Ag/Pd$ )-loaded aqueous stable  $UiO-66-NH_2$  MOF-based photocatalysts. Moreover, the  $Ag/Pd$  noble bimetallic nanoparticle loading significantly improved the optical and electrochemical features of the pristine Zr-MOF, which is well reflected *via* the composite's enhanced photocatalytic performance. Hence, a thorough discussion of the underlying photocatalytic mechanism of  $Ag/Pd@UiO-66-NH_2$  is imperative. Furthermore, the mechanism of photocatalytic  $H_2O_2$  and  $H_2$  production over the  $Ag/Pd@UiO-66-NH_2$  surface can be posited by considering the following factors:

(i) Photoresponsive factor: the  $Ag/Pd$  bimetallic-loaded  $UiO-66-NH_2$  composites are comparatively more photoresponsive in comparison to their pristine  $UiO-66-NH_2$  or monometallic counterparts, as confirmed from UV-Vis DRS analysis.<sup>29</sup> This enhanced photoresponsive factor improves the photon-trapping ability, leading to the optimal formation of excitons for effective photocatalytic redox reactions.

(ii) Improved exciton antirecombination: as photoinduced excitons are the important active species towards any photocatalytic redox reaction, their improved lifetime is pivotal for superior photocatalytic performance. Here, the  $Ag/Pd$  bimetallic-loaded  $UiO-66-NH_2$  composites have better exciton segregation tendency because of the electron-trapping ability of the bimetallic catalysts, *i.e.*,  $Ag/Pd$ .<sup>39,44</sup>

(iii) Availability of active metal centres: the  $Ag/Pd$  bimetallic nanoparticle-loaded  $UiO-66-NH_2$  composites have surplus

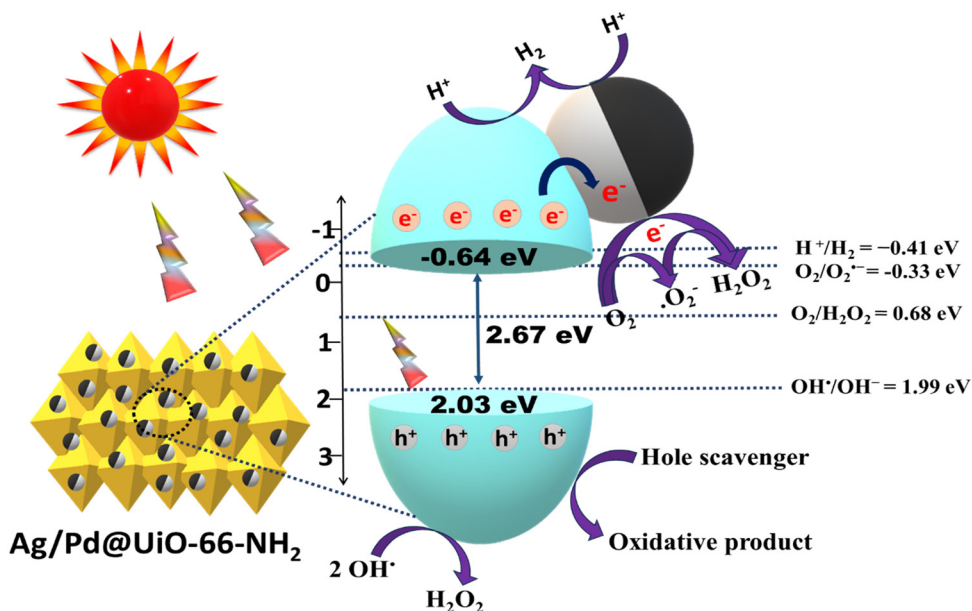
electron-rich noble metal-based active centres, *i.e.*,  $Ag/Pd$  nanoparticles tend to provide suitable reaction sites for the photocatalytic reduction reaction. Thus, the noble-metal-loaded MOFs show comparatively better photocatalytic performance, even with the decreased surface area.<sup>29,34</sup>

(iv) LSPR effect:  $Ag$  nanoparticles can strongly absorb light because of their plasmonic properties, which is further enhanced *via* the  $Pd$  support. Therefore, in  $Ag/Pd$ -loaded  $UiO-66-NH_2$ , enhanced light absorption will occur, which ultimately helps to accelerate the photocatalytic reaction as well as exciton formation. In the present research, this approach proved beneficial towards the improved photocatalytic formation of  $H_2$  and  $H_2O_2$ .<sup>34,44</sup>

(v) Suitable band edge potential:  $UiO-66-NH_2$  has  $VB = 2.03$  eV and  $CB = -0.64$  eV. This band edge potential is suitable for the studied application to show redox reactions. However, the presence of metallic components like  $Ag$  and/or  $Pd$  further enhances the reaction rate by capturing the photoexcited electrons, thereby improving their availability for the target reactions.<sup>45</sup>

Based on these physicochemical factors, as explained on the basis of suitable instrumental characterization, the superiority in efficiency of  $Ag/Pd@UiO-66-NH_2$  over its pristine  $UiO-66-NH_2$  counterpart towards photocatalytic  $H_2$  evolution and  $H_2O_2$  production has been discussed. The UV-DRS spectra show that the absorption of  $Ag/Pd@UiO-66-NH_2$  is significantly boosted in the visible light region, suggesting that the  $Ag/Pd$  bimetal loaded on the MOF surface plays a vital role in the higher absorption of visible light.<sup>34</sup> The co-existence of  $Ag/Pd$  was further confirmed by the XPS data and energy-dispersive X-ray (EDAX) spectra of the noble bimetallic NPs. The probable mechanism for the photocatalytic performance of  $Ag/Pd@UiO-66-NH_2$  towards  $H_2O_2$  and  $H_2$  production under UV-Vis light illumination is depicted in Scheme 2. As shown from UV-Vis DRS results, the absorption of  $Ag/Pd@UiO-66-NH_2$  is significantly increased in the visible light area, suggesting that the noble bimetal loaded on the surface of the MOF plays a significant role in the increased absorption of visible light. From the Tauc plot, the band gap of  $UiO-66-NH_2$  was found to be 2.67 eV. Upon irradiation of visible light, the electrons from the VB of  $UiO-66-NH_2$  get excited to the CB position. Following that, the electrons accumulate at the bimetallic surface, which acts as the electron-trapping agent and forms a Schottky barrier at the interface region between the MOF and the bimetallic NPs, which suppresses the recombination of exciton pairs. Additionally, the LSPR effect was observed due to the  $Ag$  nanoparticles, which enhanced the light-harvesting ability of the composite materials. The LSPR effect can produce a strong local electromagnetic field that can increase the energy and transfer rate of trapped electrons, facilitating easier reactions with  $h^+$  to produce  $H_2$ .<sup>44</sup> The Mott–Schottky analysis showed the VB and CB potential of  $UiO-66-NH_2$  to be 2.03 and  $-0.64$  eV, respectively. Following photon absorption, the electrons in the VB are energised and move to the CB of the  $UiO-66-NH_2$ , leaving a hole in the VB. As shown by the PL, TRPL, and EIS analyses, the presence of  $Ag/Pd$  bimetallic nanoparticles on the MOF



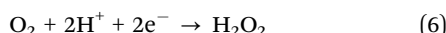


Scheme 2 Schematic representation of the mechanistic pathway for  $\text{H}_2\text{O}_2$  and  $\text{H}_2$  evolution by the prepared photocatalyst.

surface causes the excited electrons from the CB of the UiO-66-NH<sub>2</sub> to further transfer to the bimetallic surface to enhance the surface reaction more effectively and increase the exciton lifetime. When Ag/Pd is loaded onto the MOF, it helps to capture electrons from the material's surface, which enhances the photocatalytic reaction by charge carrier antirecombination in the material. Therefore, the Ag/Pd bimetallic surface essentially functions as an electron-trapping agent and aids in charge carrier separation, which is considered as the driving force for achieving the photocatalytic reaction.<sup>29</sup>

Mechanistically,  $\text{H}_2\text{O}_2$  production can be carried out *via* two pathways, *i.e.*, one-electron and two-electron pathways, as discussed subsequently. The CB potential of UiO-66-NH<sub>2</sub> (−0.64 eV) satisfies the  $\text{H}_2\text{O}_2$  production as the minimum required potentials for  $\text{H}_2\text{O}_2$  production through the oxygen reduction reaction are −0.33 eV (*via* the one-electron pathway) and 0.68 eV (*via* the two-electron pathway). Hence, the electrons transferred from the MOF surface to the bimetallic surface promote the reduction of  $\text{O}_2$  by accepting electrons from the CB of UiO-66-NH<sub>2</sub>, as shown in eqn (6) and (7):<sup>1,3</sup>

Single-step two-electron reduction pathway:



Two-step single-electron reduction pathway:



Moreover, the photogenerated  $\text{h}^+$  at the VB of UiO-66-NH<sub>2</sub> gets trapped by the sacrificial reagent, *i.e.*, isopropanol (IPA). Additionally, the VB potential of UiO-66-NH<sub>2</sub> (2.03 eV) satisfies the hydroxyl radical ( $\text{OH}^\bullet$ ) formation ( $\text{OH}^\bullet/\text{OH}^- = 1.99$  eV *vs.* NHE). Therefore, the two  $\text{OH}^\bullet$  radicals participate in the  $\text{H}_2\text{O}_2$  production, as shown in eqn (8):<sup>5,46,47</sup>

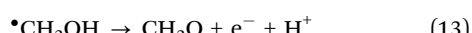
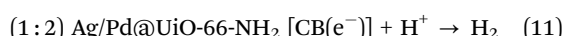
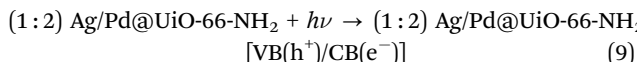


The optimal  $\text{H}_2\text{O}_2$  evolution rate of 39.44  $\mu\text{mol h}^{-1}$  was obtained for (1:2) Ag/Pd@UiO-66-NH<sub>2</sub>. Furthermore, a recyclability test was executed to check the stability of the prepared sample and it was found the material is stable for up to four cycles, as shown in Fig. 5(b). Moreover, to check the competitiveness of the reactive species towards  $\text{H}_2\text{O}_2$  production, scavenger tests were performed, as shown in Fig. 5(d). From the analysis, it was found that the contribution of active species follows the order;  $\text{e}^- > \cdot\text{O}_2^- > \text{OH}^\bullet > \text{h}^+$  to show the role towards the formation of  $\text{H}_2\text{O}_2$ .

Additionally, the synthesized materials were further tested towards the photocatalytic  $\text{H}_2$  evolution reaction. A thorough investigation was conducted to explain the increased photocatalytic activity towards the evolution of  $\text{H}_2$  gas for the Ag/Pd@UiO-66-NH<sub>2</sub> composite. Upon light irradiation, the electrons get excited to the CB of the MOF. These photogenerated electrons will go to the bimetallic surface due to the SPR effect of Ag NPs, which offers a driving force for  $\text{H}_2$  evolution.<sup>34,39</sup> The protons are reduced by the electrons present at the bimetallic surface, resulting in the production of molecular hydrogen. At the same time, holes present at the VB of UiO-66-NH<sub>2</sub> are scavenged by methanol to inhibit the exciton recombination process. Moreover, as the CB of UiO-66-NH<sub>2</sub> has a suitable redox potential, the photocatalytic formation of  $\text{H}_2$  molecule can also be observed here, as shown in Scheme 2 and eqn (9)–(14). The optimum  $\text{H}_2$  evolution rate of 448.2  $\mu\text{mol h}^{-1}$  was obtained for (1:2) Ag/Pd@UiO-66-NH<sub>2</sub>. A recyclability test was also carried out to check the stability of the material and it was found the material is stable for up to four cycles, as shown in Fig. 6(b). Moreover, the post-photocatalytic XRD analysis of the used samples showed no significant changes, suggesting



framework stability of the prepared composite, which is inherited from the parent Zr-carboxylate-based MOF. The related reaction involving hydrogen evolution is represented in eqn (9)–(14).



## 6. Summary

Initially, the  $\text{UiO-66-NH}_2$  framework was prepared by a solvothermal approach using Zr and aminoterephthalic acid as its constituents. This Zr-MOF is popular due to its abundant active sites, high surface area, visible-light-responsive band gap, and robust framework stability. However, the rapid rate of photo-generated exciton recombination as well as the relatively limited photon capture tendency of the pristine  $\text{UiO-66-NH}_2$  prevents it from becoming an efficacious photocatalyst towards photocatalytic  $\text{H}_2\text{O}_2$  and  $\text{H}_2$  production. In an attempt to boost the photocatalytic performance of pristine  $\text{UiO-66-NH}_2$ , the framework was loaded with noble bimetallic nanoparticles that act as a co-catalyst. The Ag/Pd-co-catalyst-modified MOF was engineered *via* facile adsorption–reduction method. Physico-chemical analyses including XRD, FTIR, XPS, and BET suggested the successful loading Ag/Pd nanoparticles on the  $\text{UiO-66-NH}_2$  surface accompanied with the preservation of the framework structure. Moreover, morphological analysis further corroborated the above results. The bimetallic nanoparticle-loaded composite (1:2) Ag/Pd@ $\text{UiO-66-NH}_2$  exhibited significantly enhanced photocatalytic  $\text{H}_2$  ( $448.2 \mu\text{mol h}^{-1}$ ) and  $\text{H}_2\text{O}_2$  ( $39.4 \mu\text{mol h}^{-1}$ ) production capacity that is almost four-fold higher than that of the pristine  $\text{UiO-66-NH}_2$ . Additionally the photoactivity of the Ag/Pd@ $\text{UiO-66-NH}_2$  composite was almost double those of the monometallic nanoparticle counterparts (Ag@ $\text{UiO-66-NH}_2$  or Pd@ $\text{UiO-66-NH}_2$ ). The superior output of the Ag/Pd@ $\text{UiO-66-NH}_2$  composite can be attributed to the improved photon entrapment ability *via* Pd/Ag combinatorial support, as seen from their UV-Vis spectra. Additionally, the Ag/Pd@ $\text{UiO-66-NH}_2$  composite displays superior exciton separation compared to the pristine  $\text{UiO-66-NH}_2$ , as demonstrated by the PL, TRPL, and EIS analyses. Mechanistically, the band structure of the parent MOF (VB: 2.03 eV and CB: -0.64 eV) makes it suitable for both  $\text{H}_2$  and two-step  $\text{H}_2\text{O}_2$  production. Additionally, a highly rectifying Schottky barrier with the right height is formed by bimetallic Ag/Pd nanoparticle loading, which reduces the rate of  $\text{e}^-/\text{h}^+$  recombination. In addition, the Ag component enhances the visible light absorption

through the LSPR effect with the Pd support. Meanwhile, the bimetallic surface was able to readily capture photogenerated electrons from the photon-activated  $\text{UiO-66-NH}_2$ , which is further promoted by the Ag(0) and Pd(0) of the bimetallic NPs, which suppress the charge carrier recombination. In summary, the addition of Ag/Pd bimetallic NPs on the MOF surface encourages visible light absorption and electron–hole antirecombination, leading to improved  $\text{H}_2\text{O}_2$  and  $\text{H}_2$  production.

## Conflicts of interest

The authors declare that there is no conflict of interest.

## Acknowledgements

The S ‘O’ A (Deemed to be University) management are very much thankfully acknowledged for encouragement and constant support in the research work.

## References

1. A. Ray, S. Subudhi, S. P. Tripathy, L. Acharya and K. Parida, *Adv. Mater. Interfaces*, 2022, **9**, 2201440.
2. H. Hou, X. Zeng and X. Zhang, *Angew. Chem., Int. Ed.*, 2020, **59**, 17356–17376.
3. L. Acharya, G. Swain, B. P. Mishra, R. Acharya and K. Parida, *ACS Appl. Energy Mater.*, 2022, **5**, 2838–2852.
4. Y. Guo, X. Tong and N. Yang, *Nanomicro Lett.*, 2023, **15**, 77.
5. B. P. Mishra, L. Biswal, S. Das, L. Acharya and K. Parida, *Langmuir*, 2023, **39**, 957–971.
6. Y. Xu, Y. Cao, L. Tan, Q. Chen and Y. Fang, *J. Colloid Interface Sci.*, 2023, **633**, 323–332.
7. H. Wang, L. Zhang, Z. Chen, J. Hu, S. Li, Z. Wang, J. Liu and X. Wang, *Chem. Soc. Rev.*, 2014, **43**, 5234–5244.
8. X. Chen, S. Shen, L. Guo and S. S. Mao, *Chem. Rev.*, 2010, **110**, 6503–6570.
9. J. Luo, S. Zhang, M. Sun, L. Yang, S. Luo and J. C. Crittenden, *ACS Nano*, 2019, **13**, 9811–9840.
10. B. Li, W. Guo, X. F. Lu, Y. Hou, Z. Ding and S. Wang, *Mater. Rep.: Energy*, 2023, **3**, 100203.
11. Z. Xie, W. Wang, X. Ke, X. Cai, X. Chen, S. Wang, W. Lin and X. Wang, *Appl. Catal., B*, 2023, **325**, 122312.
12. H. C. Zhou, J. R. Long and O. M. Yaghi, *Chem. Rev.*, 2012, **112**, 673–674.
13. S. P. Tripathy, S. Subudhi and K. Parida, *Coord. Chem. Rev.*, 2021, **434**, 213786.
14. S. Subudhi, S. P. Tripathy and K. Parida, *Inorg. Chem. Front.*, 2021, **8**, 1619–1636.
15. J. D. Xiao and H. L. Jiang, *Acc. Chem. Res.*, 2019, **52**, 356–366.
16. S. Prakash Tripathy, S. Subudhi, S. Das, M. Kumar Ghosh, M. Das, R. Acharya, R. Acharya and K. Parida, *J. Colloid Interface Sci.*, 2022, **606**, 353–366.
17. S. Subudhi, S. Mansingh, G. Swain, A. Behera, D. Rath and K. Parida, *Inorg. Chem.*, 2019, **58**, 4921–4934.



18 S. Subudhi, L. Paramanik, S. Sultana, S. Mansingh, P. Mohapatra and K. Parida, *J. Colloid Interface Sci.*, 2020, **568**, 89–105.

19 J. Fu and Y. Nan Wu, *Chem. – Eur. J.*, 2021, **27**, 9967–9987.

20 S. Subudhi, S. P. Tripathy and K. Parida, *Catal. Sci. Technol.*, 2021, **11**, 392–415.

21 B. Banerjee, V. Amoli, A. Maurya, A. K. Sinha and A. Bhaumik, *Nanoscale*, 2015, **7**, 10504–10512.

22 S. Chatterjee, S. Shaymal, M. Mukherjee, D. Halder, S. Chongdar, A. Paul and A. Bhaumik, *ChemSusChem*, 2022, **15**, e202200114.

23 M. Duan, L. Jiang, G. Zeng, D. Wang, W. Tang, J. Liang, H. Wang, D. He, Z. Liu and L. Tang, *Appl. Mater. Today*, 2020, **19**, 100564.

24 N. Sachi, A. P. Singh and M. Thirumal, *ACS Omega*, 2021, **6**, 34771–34782.

25 X. Sun, F. Li, Z. Wang, H. An, W. Xue and Y. Wang, *ChemCatChem*, 2021, **14**, e202101528.

26 R. Nazir, P. Fageria, M. Basu and S. Pande, *J. Phys. Chem. C*, 2017, **121**, 19548–19558.

27 S. P. Tripathy, S. Subudhi, A. Ray, P. Behera, A. Bhaumik and K. Parida, *Langmuir*, 2022, **38**, 1766–1780.

28 S. P. Tripathy, S. Subudhi, A. Ray, P. Behera, J. Panda, S. Dash and K. Parida, *J. Colloid Interface Sci.*, 2023, **629**, 705–718.

29 S. Subudhi, S. Mansingh, S. P. Tripathy, A. Mohanty, P. Mohapatra, D. Rath and K. Parida, *Catal. Sci. Technol.*, 2019, **9**, 6585–6597.

30 S. P. Tripathy, S. Subudhi, A. Ray, P. Behera, G. Swain, M. Chakraborty and K. Parida, *Langmuir*, 2023, **39**, 7294–7306.

31 S. T. Gao, W. Liu, C. Feng, N. Z. Shang and C. Wang, *Catal. Sci. Technol.*, 2016, **6**, 869–874.

32 S. Subudhi, G. Swain, S. P. Tripathy and K. Parida, *Inorg. Chem.*, 2020, **59**, 9824–9837.

33 Z. Wang, H. Lee, J. Chen, M. Wu, D. Y. C. Leung, C. A. Grimes, Z. Lu, Z. Xu and S. P. Feng, *J. Power Sources*, 2020, **466**, 228306.

34 I. Majeed, U. Manzoor, F. K. Kanodarwala, M. A. Nadeem, M. A. Nadeem, E. Hussain, H. Ali, A. Badshah and J. A. Stride, *Catal. Sci. Technol.*, 2018, **8**, 1183–1193.

35 O. Altan and E. Kalay, *Appl. Surf. Sci.*, 2022, **580**, 152287.

36 Y. Z. Chen, Y. X. Zhou, H. Wang, J. Lu, T. Uchida, Q. Xu, S. H. Yu and H. L. Jiang, *ACS Catal.*, 2015, **5**, 2062–2069.

37 J. Ma, X. Yu, X. Liu, H. Li, X. Hao and J. Li, *Mol. Catal.*, 2019, **476**, 110533.

38 D. Tan, J. Zhang, J. Shi, S. Li, B. Zhang, X. Tan, F. Zhang, L. Liu, D. Shao and B. Han, *ACS Appl. Mater. Interfaces*, 2018, **10**, 24516–24522.

39 C. Liu, Y. Zhang, J. Wu, H. Dai, C. Ma, Q. Zhang and Z. Zou, *J. Mater. Sci. Technol.*, 2022, **114**, 81–89.

40 J. Qin, J. Huo, P. Zhang, J. Zeng, T. Wang and H. Zeng, *Nanoscale*, 2016, **8**, 2249–2259.

41 N. Hintsho, L. Petrik, A. Nechaev, S. Titinchi and P. Ndungu, *Appl. Catal., B*, 2014, **156–157**, 273–283.

42 F. S. Hashim, A. F. Alkaim, S. J. Salim and A. H. O. Alkhayatt, *Chem. Phys. Lett.*, 2019, **737**, 136828.

43 Y. Peng, L. Wang, Y. Liu, H. Chen, J. Lei and J. Zhang, *Eur. J. Inorg. Chem.*, 2017, 4797–4802.

44 M. A. Nadeem, M. Al-Oufi, A. K. Wahab, D. Anjum and H. Idriss, *ChemistrySelect*, 2017, **2**, 2754–2762.

45 S. P. Tripathy, S. Subudhi, A. Ray, P. Behera, G. Swain, M. Chakraborty and K. Parida, *Langmuir*, 2023, **39**, 7294–7306.

46 H. Zhang and X. Bai, *Appl. Catal., B*, 2021, **298**, 120516.

47 X. Wang, Z. Han, L. Yu, C. Liu, Y. Liu and G. Wu, *ACS Sustainable Chem. Eng.*, 2018, **6**, 14542–14553.